Electronic Supplementary Material (ESI) for Journal of Materials Chemistry C.

Effect of methoxy-substitutions on the hole transport properties of carbazole-based compounds: pros and cons

Seyhan Salman[a], Xavier Sallenave[b], Audrius Bucinskas[c], Dmytro Volyniuk[c], Oleksandr Bezvikonnyi[c], Viktorija Andruleviciene[c], Juozas Vidas Grazulevicius[c*], Gjergji Sini[b*]

[a]Clark Atlanta University, Department of Chemistry, 223 James P. Brawley Drive, SW, Atlanta, GA 30314.

[b]CY Cergy Paris Université, Laboratoire de Physicochimie des Polymères et des Interfaces, EA 2528, 5 mail Gay-Lussac, Cergy-Pontoise Cedex, 95031, France.

[b]Kaunas University of Technology, Department of Polymer Chemistry and Technology, Radvilenu pl. 19, LT-50254, Kaunas, Lithuania.

Supporting Information

Table S1. DFT/ω*B97XD-calculated frontier molecular orbital levels of the compounds C1-C4 and P1-P4.

Compound	E_{HOMO} (eV)	E_{LUMO} (eV)	$E_{HOMO-LUMO}$ (eV)
C1	-5.57	-0.80	4.78
C2	-5.11	-0.75	4.35
C3	-5.21	-0.72	4.49
C4	-4.94	-0.78	4.17
P1	-5.66	-0.49	5.18
P2	-5.16	-0.51	4.65
P3	-5.29	-0.51	4.78
P4	-5.02	-0.43	4.58

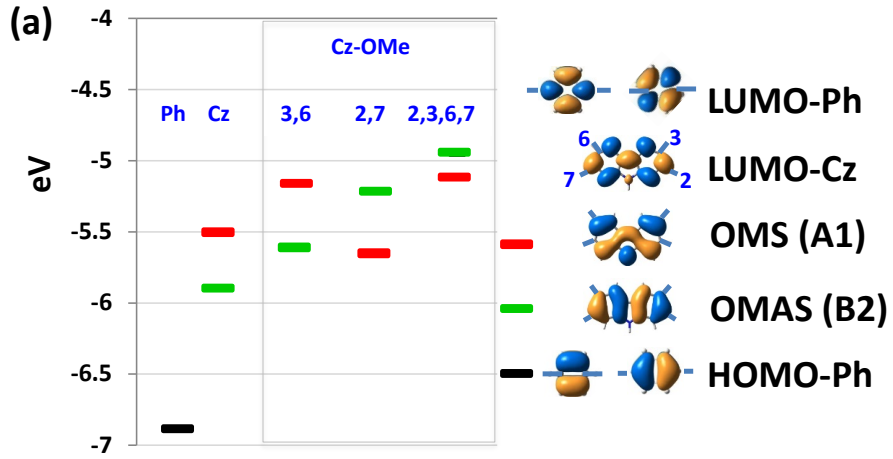
(a)
-4
-4.5
-5
-5.5
-6
-6.5
-7
eV
Cz-OMe
Ph
Cz
3,6
2,7
2,3,6,7
LUMO-Ph
LUMO-Cz
OMS (A1)
OMAS (B2)
HOMO-Ph

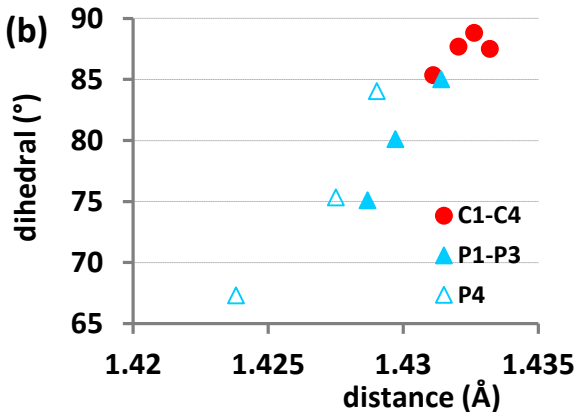
(b)
90
85
80
75
70
65
dihedral (°)
C1-C4
P1-P3
P4
1.42
1.425
1.43
1.435
distance (Å)

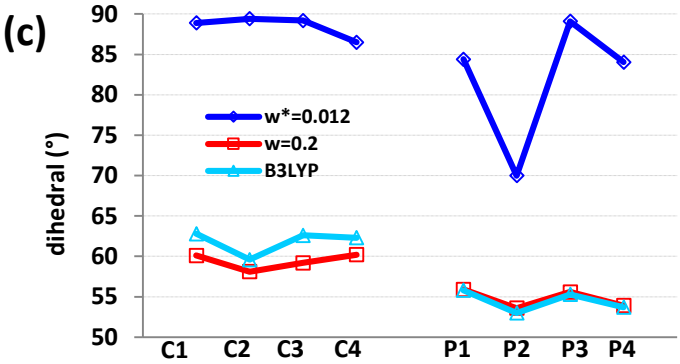
(c)
90
85
80
75
70
65
60
55
50
dihedral (°)
w*=0.012
w=0.2
B3LYP
C1
C2
C3
C4
P1
P2
P3
P4

(d)

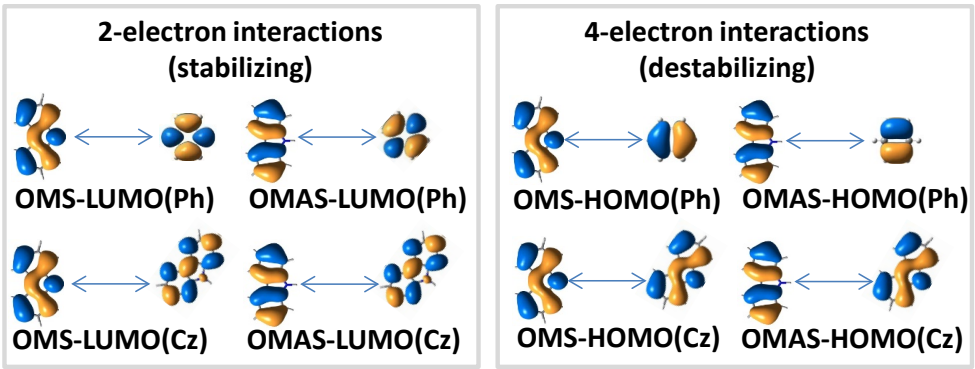
2-electron interactions
(stabilizing)
OMS-LUMO(Ph)
OMAS-LUMO(Ph)
OMS-LUMO(Cz)
OMAS-LUMO(Cz)
4-electron interactions
(destabilizing)
OMS-HOMO(Ph)
OMAS-HOMO(Ph)
OMS-HOMO(Cz)
OMAS-HOMO(Cz)

(e)

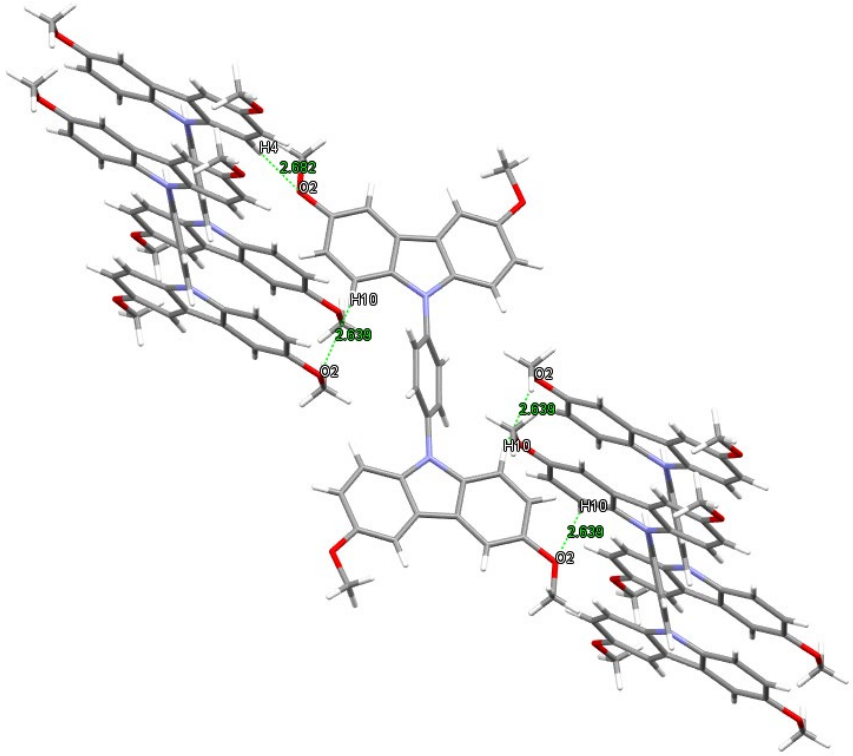

(f)

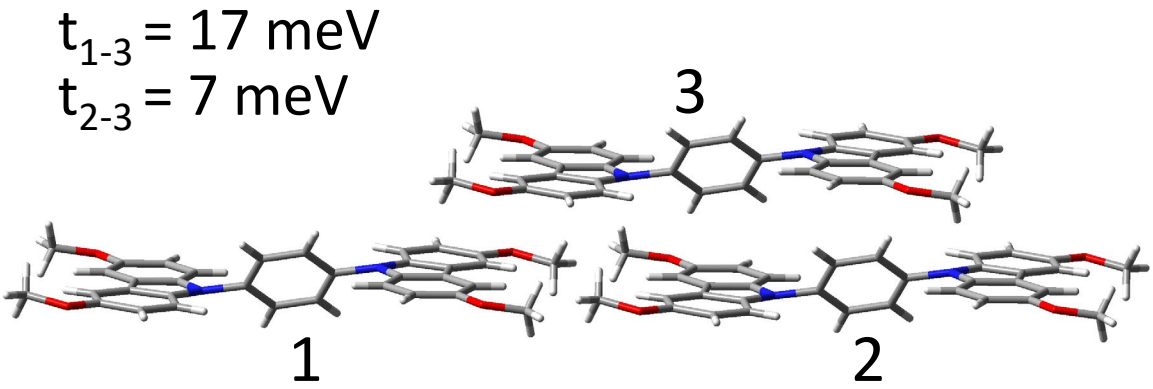

Figure S1. (a) DFT/ω*B97XD-calculated molecular orbitals of the building fragments (Ph, Cz, and Cz-OMe) in triscarbazole derivatives. Ph = Phenyl, and Cz = Carbazole. **(b)** Evolution of the dihedral angle with respect to the inter-fragment distance in C and P compounds. **(c)** Dihedral angles of compounds C1-C4 and P1-P4 calculated with different methods: the tuned-ω*B97XD functional (ω =0.012 $Å^{-1}$, see computational section, SI), the default ωB97XD (ω =0.2 $Å^{-1}$), and B3LYP functionals. **(d)** Molecular orbital inter-fragment interactions by means of the local HOMO(Cz) and HOMO-1(Cz) of the lateral carbazoles, and the local HOMO(core) and LUMO(core) of the central fragment. (e) Fragment of the crystal structure of

compound P2. The short contacts highlighted in green correspond to hydrogen bonds between adjacent molecules. The single crystal for compound **P2** was obtained using slow evaporation technique from solvent mixture (hexane:dichlormethane = 1:1). Colourless single crystal was attached on the glass capillary using glue. The experiment was performed using XtaLAB mini diffractometer (Rigaku) with graphite monochromated Mo Kα (λ = 0.71075 Å) X-ray source. The measurements were performed at room temperature (293 K). The crystallographic data for **P2** structure reported in this manuscript have been deposited in Cambridge Crystallographic Data Centre with CCDC no 2077925. The copies of data can be obtained free of charge on application to CCDC. Calculations/visualizations were performed using the OLEX2 crystallographic software package except for refinement, which was performed using SHELXL. (Dolomanov, O. V.; Bourhis L. J.; Gildea R. J.; J. Howard A. K. and Puschmann H., OLEX2: a complete structure solution, refinement and analysis program. *J. Appl. Crystallogr.*, **2009**, *42*, 339–341. Sheldrick G. M., A short history of SHELX. *Acta Crystallogr. Sect. A Found. Crystallogr.*, **2008**, *64*, 112–122. (f) Transfer integrals of the most pertinent pi-pi stacked dimers (B3LYP/6-31G(d,p) level, according to the method described in Valeev et al. JACS, 128 (30), 9882-9886). Figures (a) and (c) are reprinted from reference 29 (main text) with permission from Journal of Physical Chemistry C.

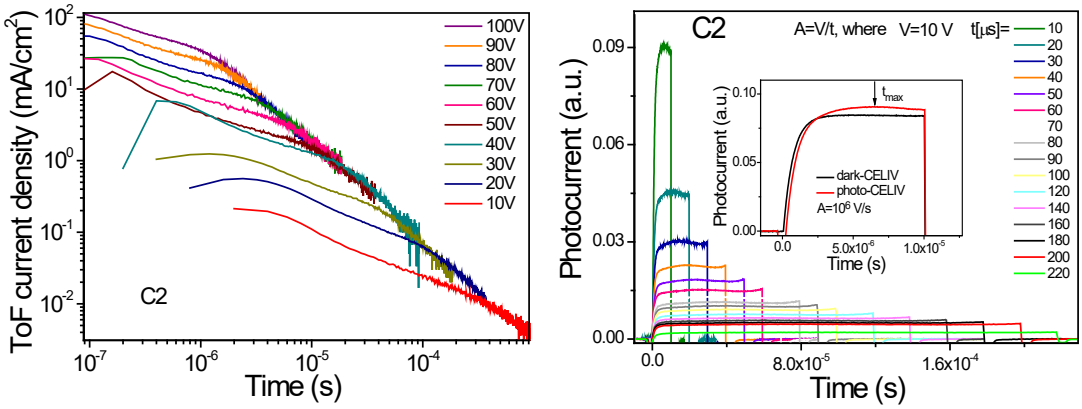

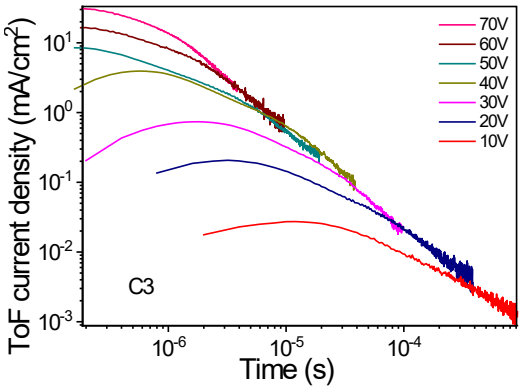
ToF current density (mA/cm²)
Time (s)
C3
70V
60V
50V
40V
30V
20V
10V

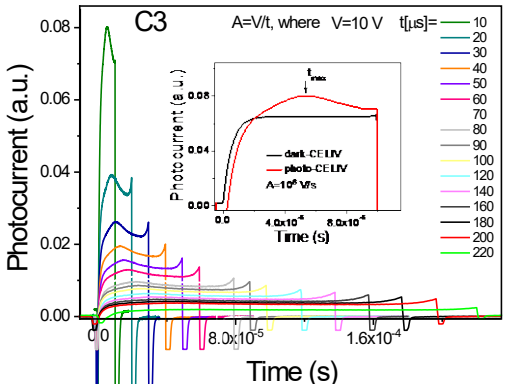
C3
A=V/t, where V=10 V t[μs]=
Photocurrent (a.u.)
Time (s)
dark-CELIV
photo-CELIV

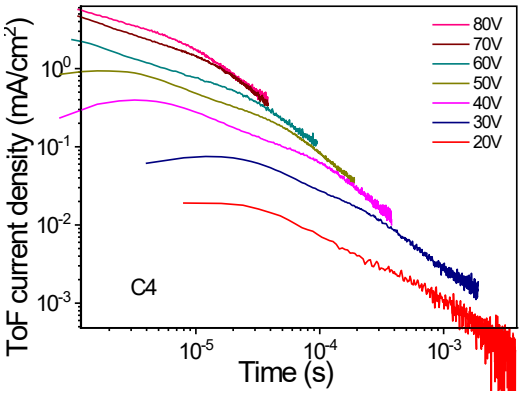
ToF current density (mA/cm²)
Time (s)
C4
80V
70V
60V
50V
40V
30V
20V

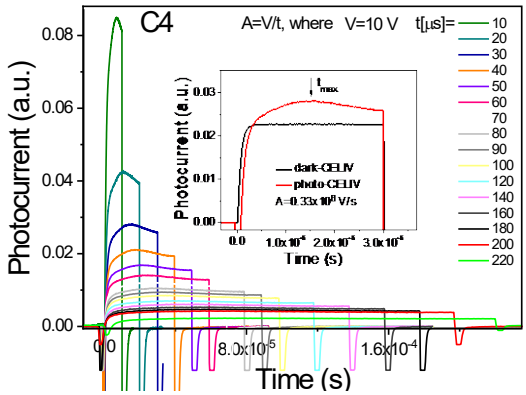
C4
A=V/t, where V=10 V t[μs]=
Photocurrent (a.u.)
Time (s)
dark-CELIV
photo-CELIV

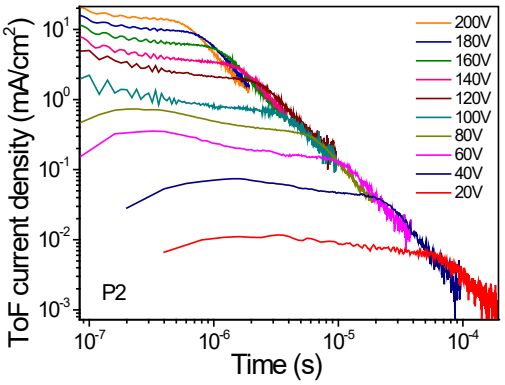
ToF current density (mA/cm²)
Time (s)
P2
200V
180V
160V
140V
120V
100V
80V
60V
40V
20V

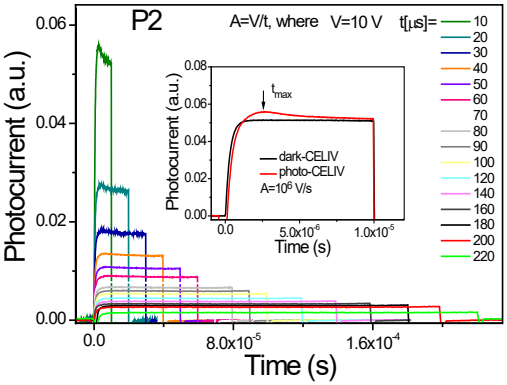
P2
A=V/t, where V=10 V t[μs]=
Photocurrent (a.u.)
Time (s)
dark-CELIV
photo-CELIV

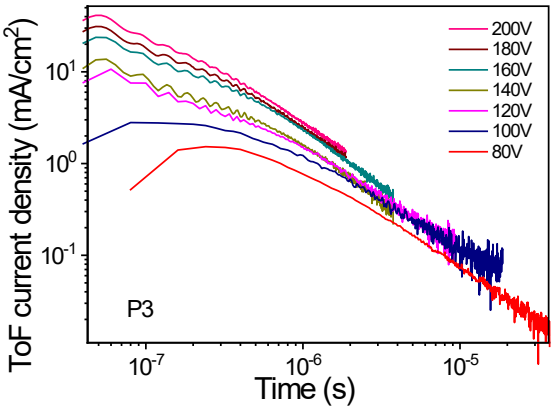
ToF current density (mA/cm²)
Time (s)
P3
200V
180V
160V
140V
120V
100V
80V

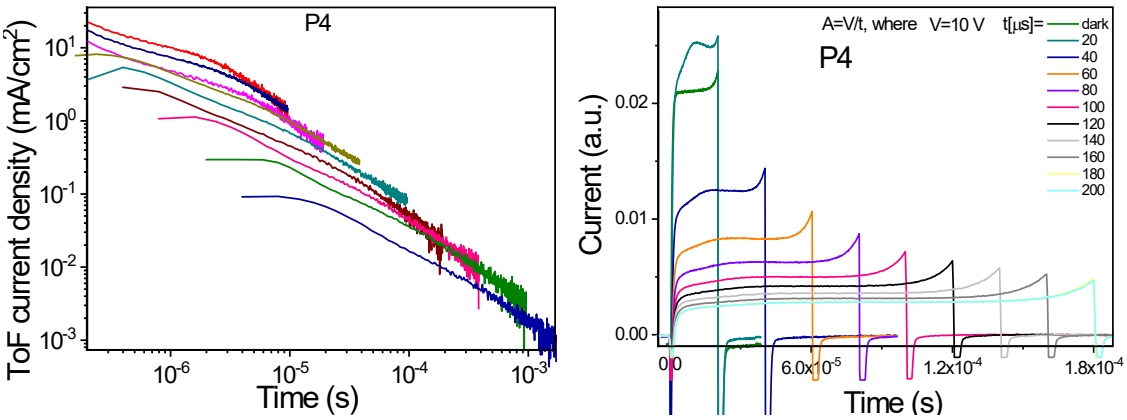

Figure S2. TOF (the left) and CELIV (the right) current transient pulses for the layers of the studied compounds C2-C4 and P1-P4 at room temperature.

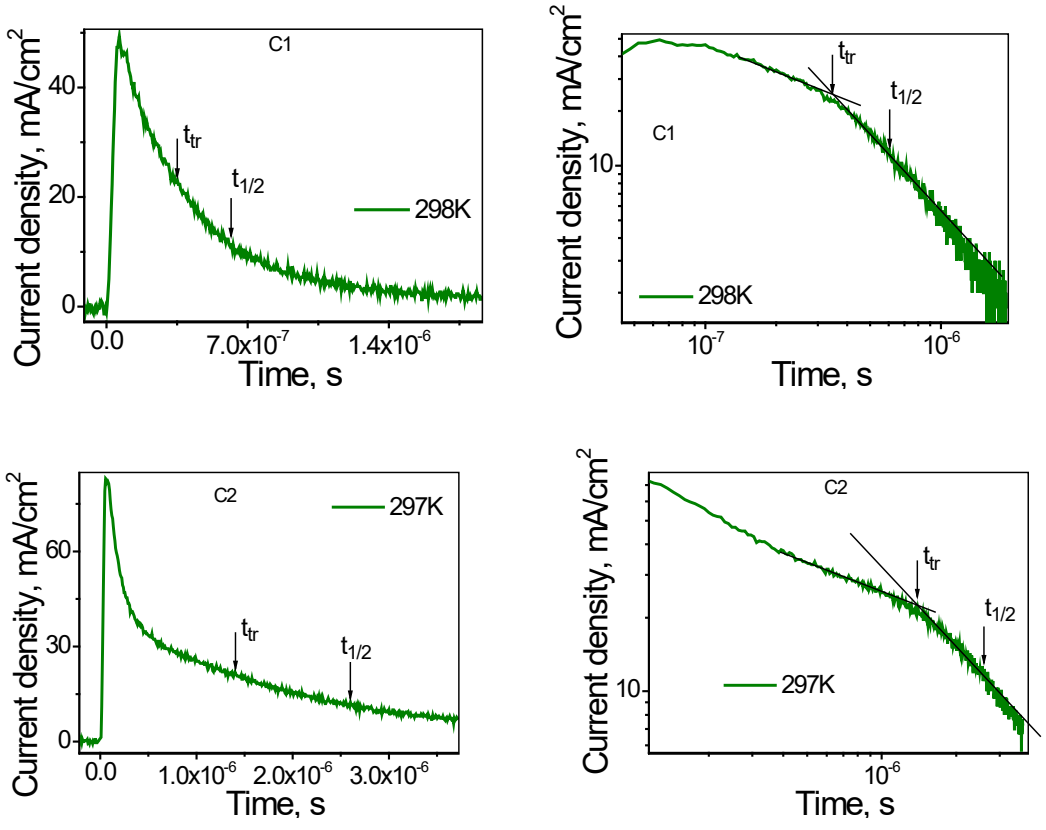

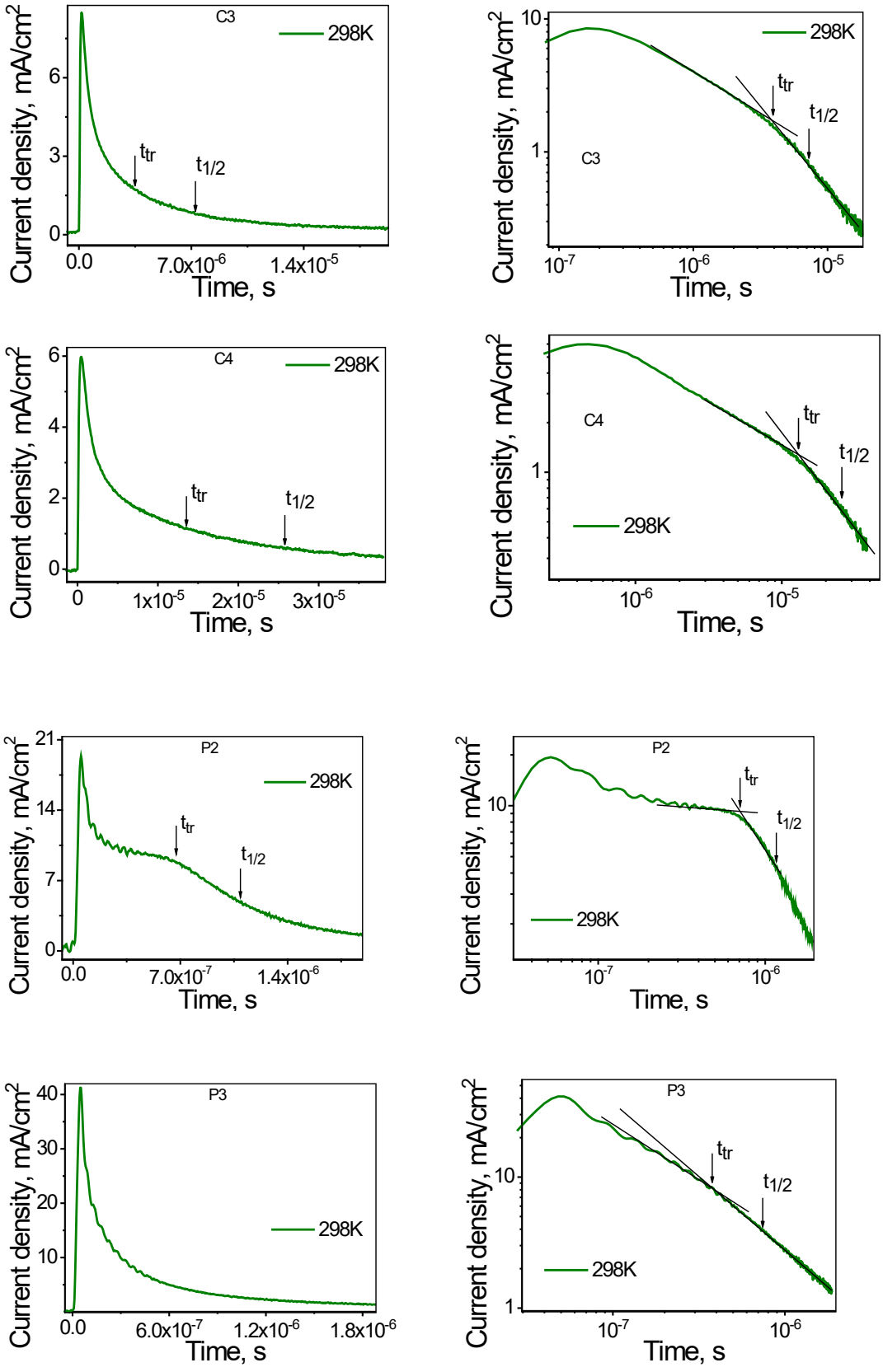

Figure S3. TOF current transient pulses for C and P compounds.

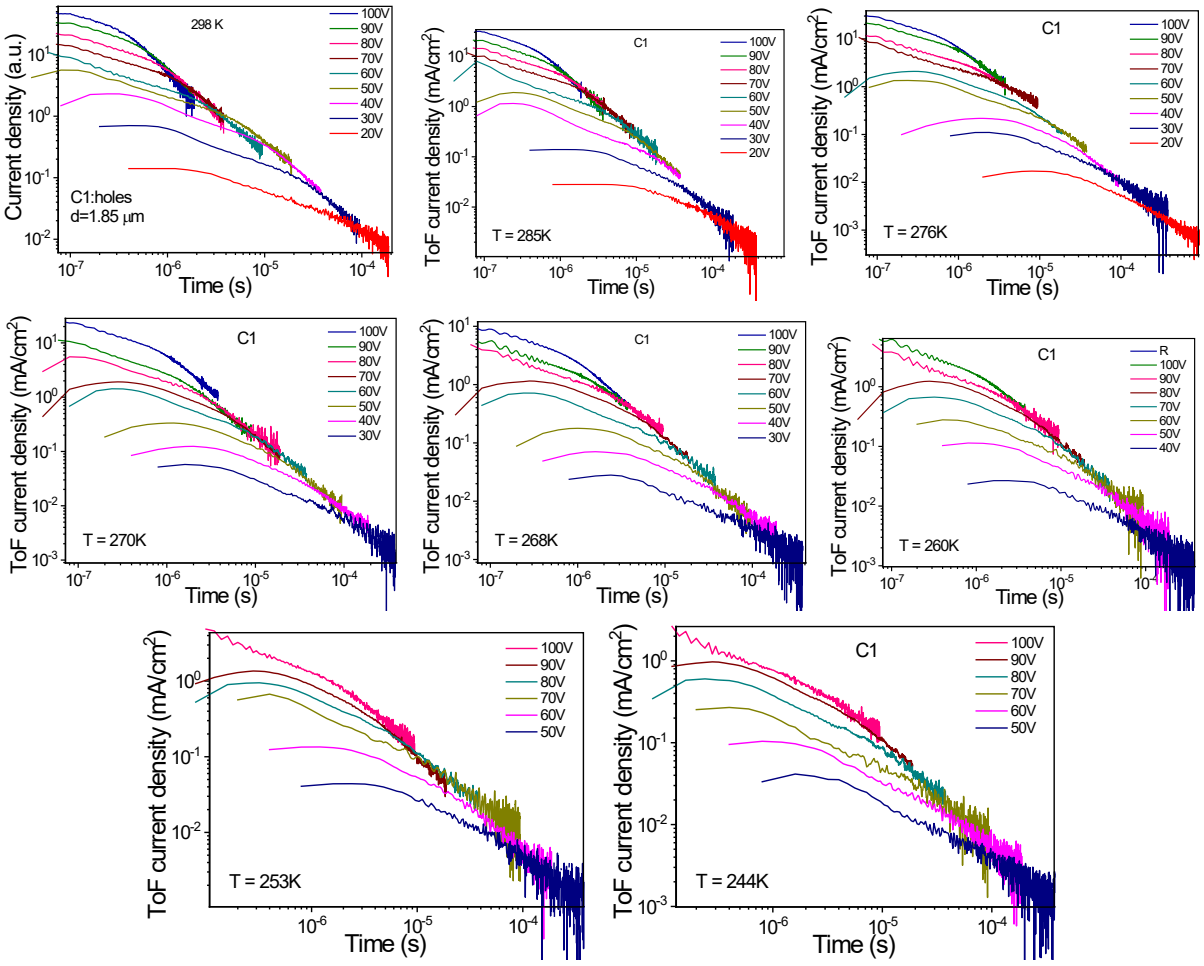

Figure S4. TOF signals for the layer C1 at different electric fields and temperatures.

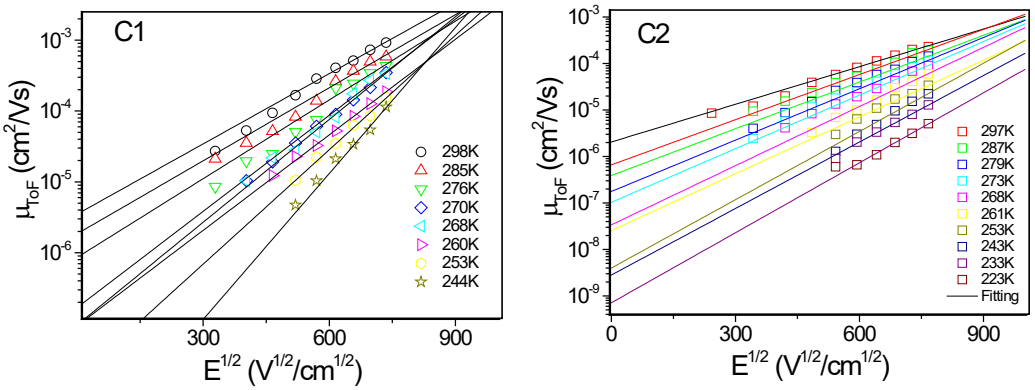

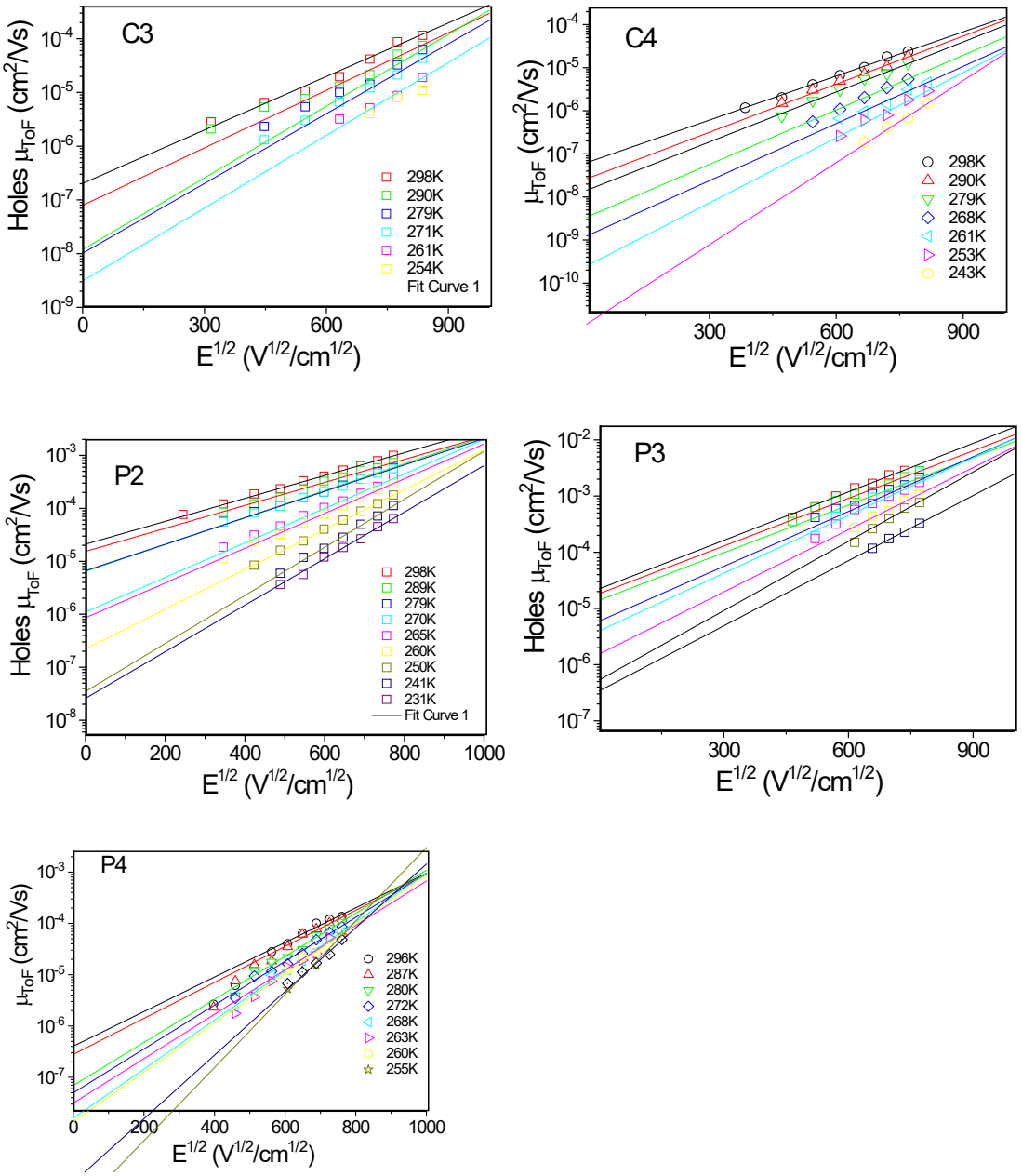

Figure S5. Electric field dependencies of the mobility for the layers of the studied compounds at the different temperatures.

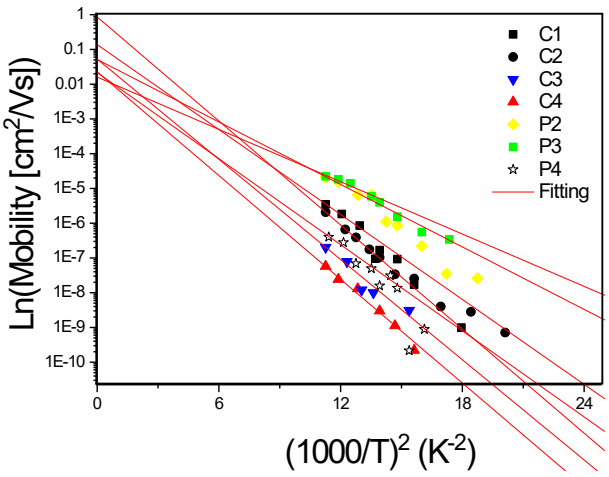

Figure S6. The logarithm of the zero-field mobility vs $(1000/T)^2$. The zero-field mobility values were obtained by the fitting of the data in **Fig. S6** as $\mu=\mu_0 \cdot exp(\beta \cdot E^{1/2})$ at the electric field E=0.

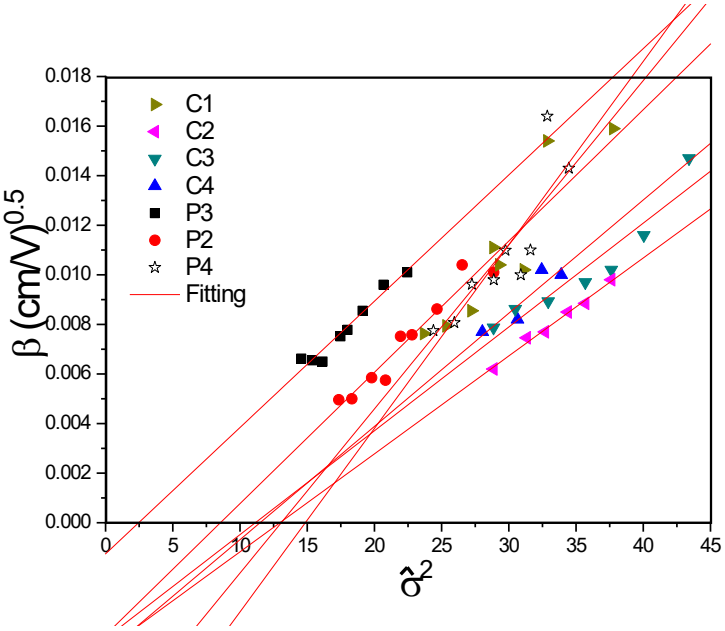

Figure S7. The temperature dependence of the field dependencies of the mobility.

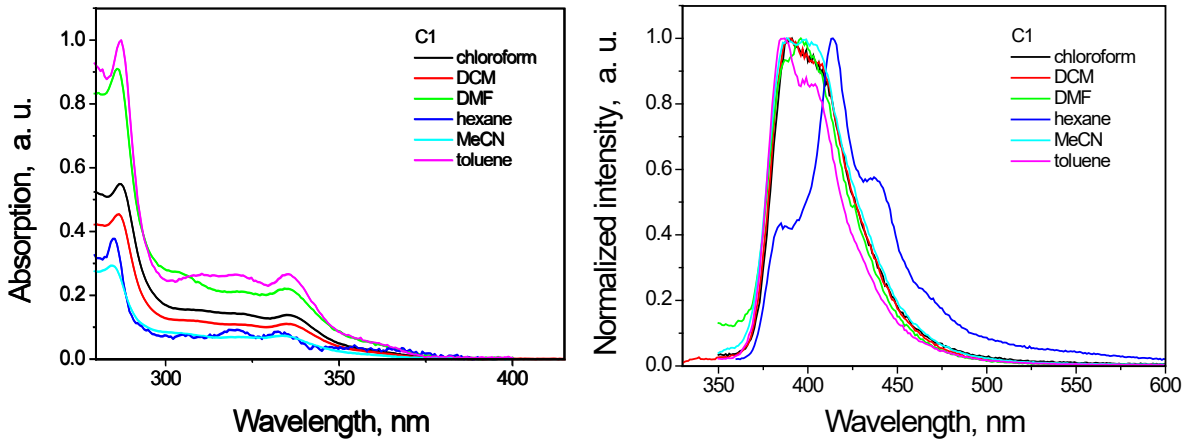

Figure S8. Absorption and PL spectra of dilute solutions of C1.

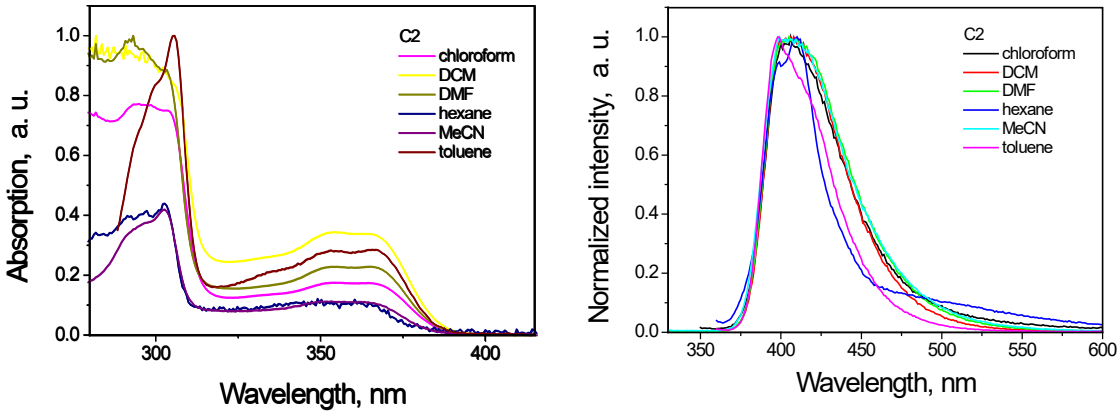

Figure S9. Absorption and PL spectra of dilute solutions of C2.

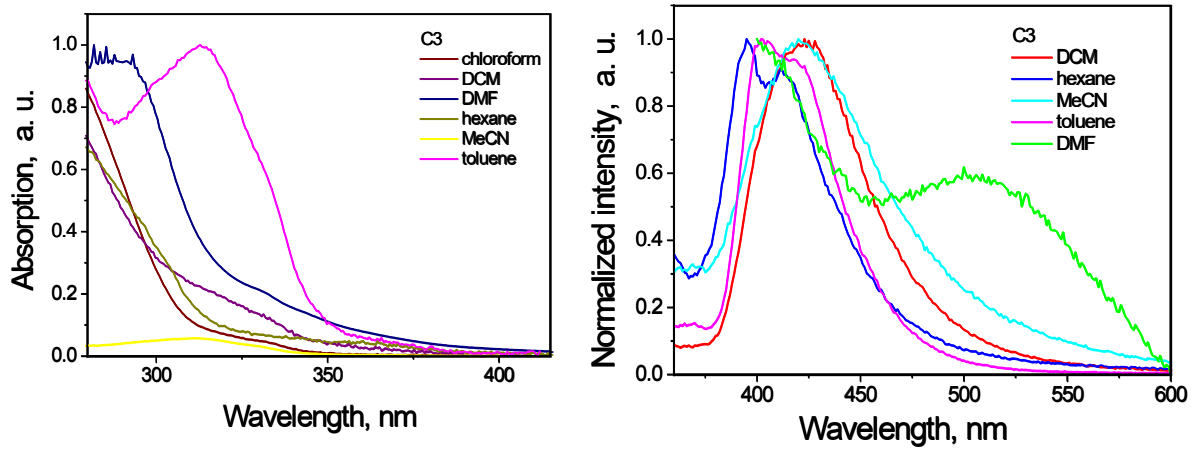

Figure S10. Absorption and PL spectra of dilute solutions of C3.

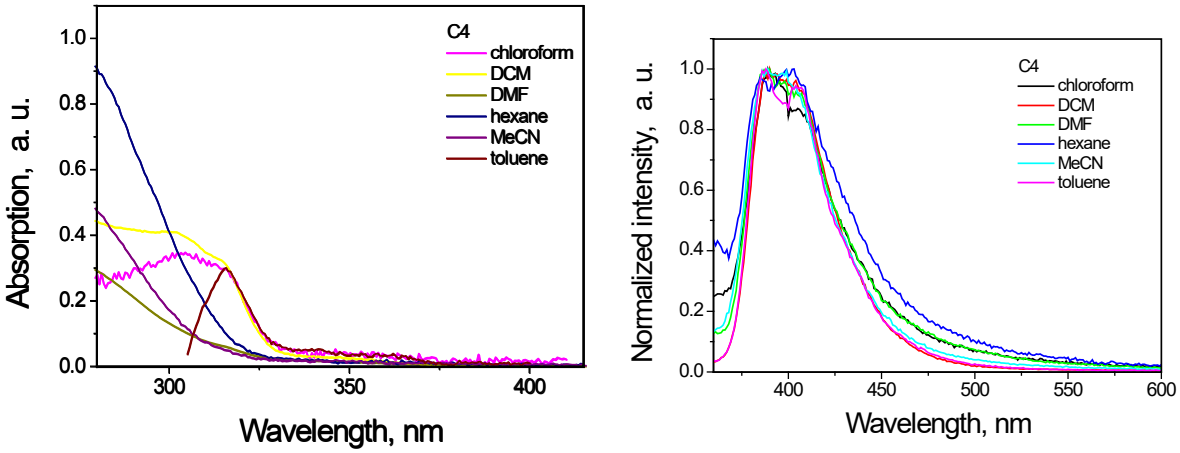

Figure S11. Absorption and PL spectra of dilute solutions of C3.

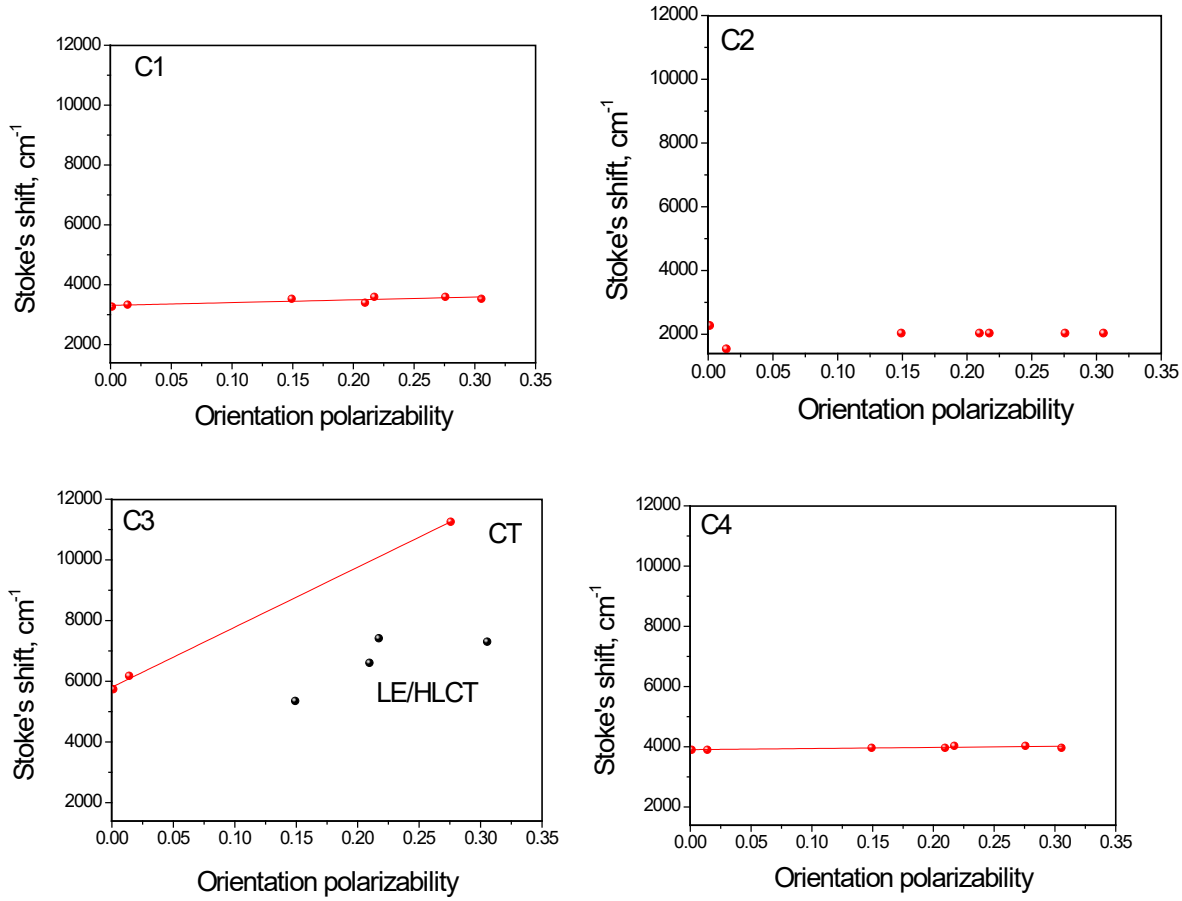

Figure S12. The Lippert-Mataga plots.

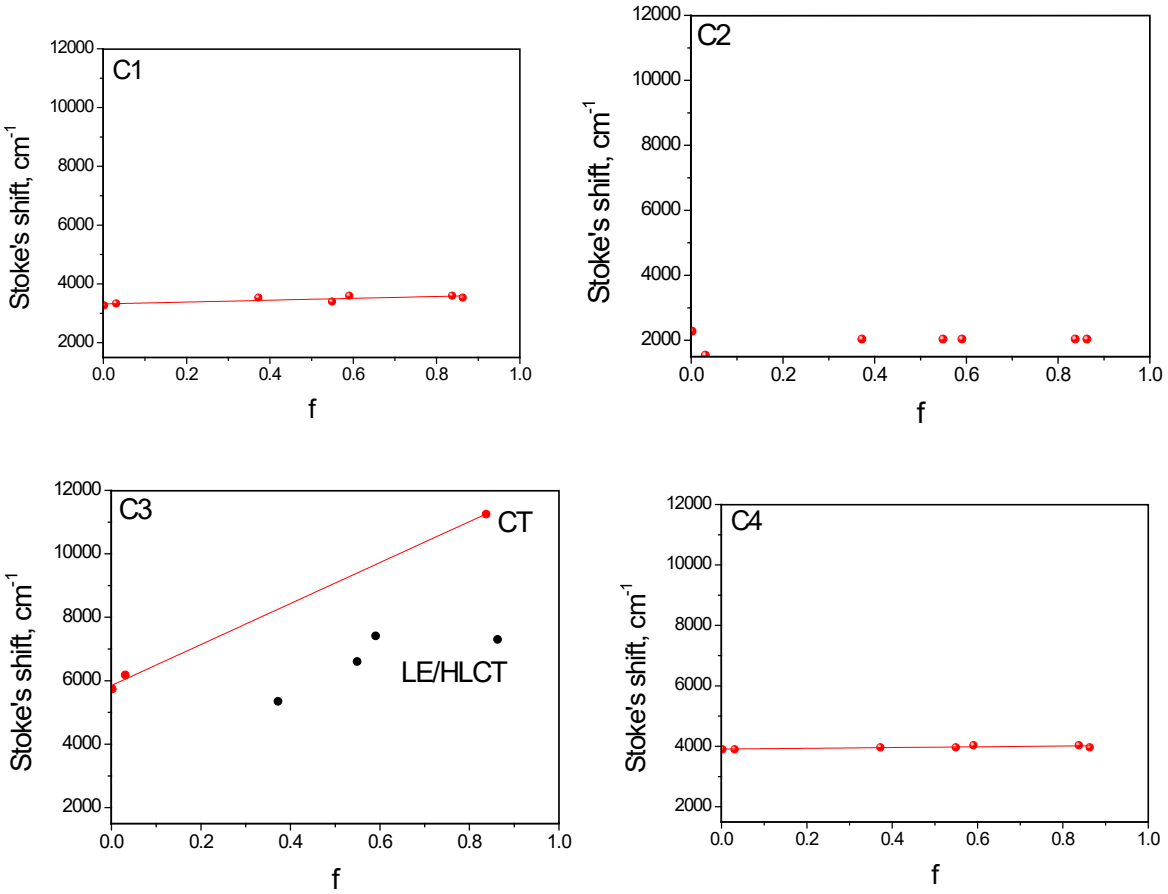

Figure S13. The plots of Bakshiev polarity function.

Annexes

Annex I. Factors impacting the inter-fragment dihedral angles

In order to analyze some factors explaining the evolution of inter-fragment dihedral angles across the two series of compounds, we firstly we check for the impact of the steric hindrance between the lateral and core fragments. As a general observation we note that, if the trend of the dihedral angles across the two series was driven by inter-fragment steric hindrance, the smallest dihedral angle would correspond to the larger inter-fragment distance. Instead, **Figure S1b** shows increasing of inter-fragment dihedral angles with the increasing inter-fragment distance, which is at odds with the dominance of the steric interactions.

In order to check for the impact of any possible steric repulsion between the two tetra-OMe-Cz groups in P4, the test half-P4 compound containing only one tetra-OMe-Cz group linked to Ph was calculated, but the resulting dihedral angle is again very small (69.4° and 79.3° with ω parameter values of 0.026 and 0.012bohr^{-1} respectively). Other test calculations on C1-C4, P1-P4, and half-P4 by employing the B3LYP functional or by increasing the ω parameter values from 0.012- to 0.2 bohr^{-1} (tuned and default respectively) result in decreasing inter-fragment dihedrals and distances (Figure S1c)), thus pointing to the impact of the inter-fragment π-conjugation efficiency.

We focus consequently on the orbital inter-fragment interactions by means of the local HOMO(Cz) and HOMO-1(Cz) of the lateral carbazoles, and the local HOMO(core) and LUMO(core) of the central fragment. In the case of Ph core, both HOMO and LUMO levels are doubly degenerate, with orbitals being symmetric- or antisymmetric with respect to the symmetry plane containing the two linking positions (**Figure S1c**).

We discuss now the evolution of the dihedral angles as a result of the competition between stabilizing HOMO(Cz)-LUMO(core) interaction (involving two electrons), and the destabilizing HOMO(Cz)-HOMO(core) interaction (involving 4 electrons). The strength of these interactions depends on (i) the symmetry of the interacting fragment orbitals, and (ii) on their energy difference.

The inter-fragment orbital interactions are schematically shown in **Figure S1c** in the limit case of the coplanar configuration (inter-fragment dihedral angle of 0°). Inspection of these orbital interactions indicates that both the stabilizing 2-electron interactions and the destabilizing 4-electron interactions (left and right panels, respectively) are of maximum overlap in the planar configuration, but become of zero overlap in the case of orthogonal configurations. Accordingly, the stabilizing 2-electron interactions favor the planar configurations, whereas the destabilizing 4-electron ones favor the orthogonal configurations. Twisted equilibrium geometry should consequently result from a trade-off between these interactions by means of OMS. As for OMAS, maximal overlaps can be deduced for both 2-electron and 4-electron interactions in both coplanar and orthogonal configurations due to the perfect symmetry matching between OMAS and HOMO(Ph) and LUMO(Ph) in these limit geometries. Interestingly, these overlaps can only decrease in the twisted configurations, again suggesting favored twisted configurations. *Both OMS and OMAS interactions favor consequently twisted configurations.* Note that the interactions through OMAS are expected to be less efficient as compared to OMS, due to the absence of contribution from the N atom.

The tradeoff between these opposite effects is importantly weighted by the energy splitting between the interacting orbitals. In view of the much larger energy differences corresponding to the stabilizing 2-electron interactions (4.5-4.8 eV) as compared to the destabilizing 4-electron ones (0.3-0.55 eV and 1.7-1.9 eV for C1-C4 and P1-P4 respectively,

Figure S1a), the equilibrium dihedral angles are expected to be dominated by the 4-electron interactions. This effect could in part explain (i) the globally large dihedrals found for these compounds, (ii) the globally smaller dihedrals in P1-P4 as compared to C1-C4 (70.1-89.1° and 86.5-89.4° respectively). Interestingly, the energy differences corresponding to the destabilizing 4-electron interactions calculated by the tuned-ω*B97XD functional are smaller by 20-46% and 34-62% as compared to the values calculated with both B3LYP or by the default ωB97XD respectively, which could in part explain the smaller dihedrals by roughly 27-36 % in the latter cases (**Figure S1a**).

Comparing now the compounds P1-P4, the trend in dihedrals P1>P3>P2≈P4 seems to correlate with the (i) decreasing OMS-LUMO(Ph) energy difference (6.01 > 5.57 > 5.52 > 5.31 eV respectively), suggesting increasing impact of the stabilizing 2-electron interactions in the same order (favoring coplanar configurations), and (ii) with the increasing OMS-HOMO(Ph) energy difference (1.25 > 1.68 > 1.74 > 1.95 eV respectively), corresponding to decreased impact of the destabilizing 4-electron interactions. In the case of compounds C1-C4 (core=carbazole), the OMS-HOMO(Ph) energy differences are smaller (0.30-0.55 eV), which could explain the globally larger dihedral angles in the C1-C4 series as compared to P1-P4.

Certainly, the above qualitative analysis is not complete, and the variations on the inter-fragment orbital overlaps cannot be accounted for in the framework of such a qualitative analysis. Indeed, it can be globally deduced that the 3,6-OMe substitutions, shifting up and preserving the OMS/OMAS order, should result in decreased dihedral angles. This seems to be the case when comparing P2 and P1, but not in the case of C2 and C1 having almost identical dihedral angles. Similarly, the 2,7-substitutions inverse the OMS/OMAS order, thus resulting in larger dihedral angles as compared to C1. This is obvious for instance in the opposite trends obtained for compounds C4 and P4 exhibiting smaller and larger dihedrals as compared to C3 and P3, respectively, directly pointing on the impact of the core orbital energy and symmetry.

The final geometry is the result of a subtle competition between all these (and other) stabilizing and destabilizing interactions, which cannot be deduced in the framework of this qualitative analysis. As such, the above analysis can only point to a global view on the factors impacting the inter-fragment dihedral angles, all results pointing to the (i) dominant impact of inter-fragment orbital interactions as compared to steric ones, (ii) interactions that are strongly impacted by the inter-fragment energy differences, and (iii) interactions in direct correlation with the topology and number of methoxy substitutions.

Annex II. Temperature dependent TOF results and analysis

The time-of-flight (TOF) method was used for investigation of both field and temperature dependencies of hole mobilities of the compounds (Figure S4-S7) [1]. To evaluate their disorder parameters, the experimental results were analyzed within the Gaussian disorder model [2]. The Gaussian disorder model predicts the field and temperature dependencies of the mobility given as:

$$\mu = \mu_0 \exp[-(\frac{2\hat{\sigma}}{3})^2]\exp[C(\hat{\sigma}^2 - \Sigma^2)E^{1/2}] \quad (1)$$

Here, σ characterizes the energy width of the hopping site manifold, and Σ is the positional disorder due to a distribution of intersite distances; C is a constant and $\hat{\sigma} = \sigma/kT$.

For example, Figure S4 shows a set of TOF signals for the layer of C1 recorded at different electric fields and temperatures. Similar dependencies were recorded for the other compounds. The Poole−Frenkel-like field dependencies of mobility μ of the studied compounds at different temperatures are collected in Figure S5. To determine the values of σ using Eq. (1), the

temperature dependencies of the zero-field mobility ($\mu_{(E=0)}$) were plotted semi-logarithmically versus $1000/T^2$ (Figure S6). The zero-field mobility values were obtained by the extrapolation of the data to the electric field E = 0 as illustrated in Figure S5. Using Eq. (1), σ can be determined from the slope of a plot of log $\mu_{(E = 0)}$ versus T^{-2}. Figure S7 shows the field dependencies of the mobilities at the different temperatures. The results are plotted as $\beta = d\ ln\mu/dE^{0.5}$ versus $\hat{\sigma}^2$. The values of Σ and C can be determined from the slope and intercept of a plot of β versus $\hat{\sigma}^2$ (Figure S7).

[1] S.C. Tse, C.H. Cheung, S.K. So in Organic Electronics Materials, Processing, Devices and Applications; Franky So Ed.; Taylor & Francis, London, 2010; Chapter 3, pp 71−74.

[2] H. Bassler, Phys. Status Solidi B 1993, 175, 15.

Annex III.

The solvatochromic effect can be investigated using descriptions of non-specific electrostatic interaction between the molecules of solute and solvent introduced by Onsager.[1] The Lippert-Mataga plot[2–4] of the dependence of Stokes shift $\Delta\tilde{\nu}$ and orientation polarizability Δf based on the Onsager model is widely used for estimation of the change of dipole moments after excitation $\mu_e - \mu_g$.

It is based on the equation (1):

$$\Delta\tilde{\nu} = \frac{2\Delta f}{4\pi\varepsilon_0\hbar c a^3}(\mu_e - \mu_g)^2 + \Delta\tilde{\nu}^0 \quad (1)$$

$$\Delta f = \frac{\varepsilon-1}{2\varepsilon+1} - \frac{n^2-1}{2n^2+1} \quad (2)$$

Superscript ^{0} indicates the absence of solvent contribution. a is the so-called Onsager cavity radius and can be evaluated using formula (3):

$$a^3 = \frac{3M}{4\pi N_A d} \quad (3),$$

where M, N_A and d are the molar mass, Avogadro constant and density, respectively.

Absorption and emission spectra of dilute solutions of C1-C4 were recorded for analysis of the solvatochromism (Fig. S8-S11, the spectra of THF solutions are taken from[5]). Absorption spectra exhibit no spectral shifts of the lowest energy band[5] upon increase of polarity of the solvent. Significantly redshifted distinctive PL spectral band assigned to the charge transfer state was detected for chloroform and DMF solutions of C3 (Fig. S10). The peak position was prominent for the DMF solution. Since PL spectra of C3 dissolved in non-polar hexane and toluene represent emission of the local excited state, these data were used for the following calculations. Interestingly, the positive solvatochromism was practically absent for C2 solutions (Fig. S9). Evidently, there is no charge transfer to get values of C2 dipole moments experimentally (Fig. S12, S13). Assuming that all the investigated compounds have the similar values of density, it was taken as 1.313 g/cm^3. a was estimated to be of ca. 5.4, 5.8 and 6.1 Å, for C1, C3 and C4 respectively. The slopes of Lippert-Mataga linear relationships correspond to the approximated values of 3.8, 19.6 and 2.9 D for C1, C3 and C4, respectively.

Alternatively, the Bakshiev polarity function[6] (4), (5) can be utilized similarly to the Lippert-Mataga plot:

$$\Delta\tilde{\nu} = \frac{2f}{4\pi\varepsilon_0\hbar c a^3}(\mu_e - \mu_g)^2 + constant \quad (4)$$

$$f = [\frac{\varepsilon-1}{\varepsilon+2} - \frac{n^2-1}{n^2+2}] \frac{(2n^2+1)}{(n^2+2)} \quad (5)$$

At the result, 2.2, 11.2 and 1.7 D were calculated from the corresponding slopes of the plots of Bakshiev polarity function for C1, C3 and C4, respectively.

Our experimental findings show that the value is negligible for C2 as no solvatochromism was observed and higher than 11 D estimated for C3 correlate well with the result of theoretical calculations. The proposed methods of estimation of μ_g and μ_e separately based on Lippert, Bakshiev, Kawasaki-Chamma-Viallet approaches are not applicable for the compounds since they are based on the assumption that dipole moments of the ground and excited states are parallel.[7] In our case the dipole moments are located at the certain angle[8] since compounds C1-C4 do not possess usual for such kind of methods donor-acceptor structure with clear spatial separation of charges. The important method which allows to make conclusion about the dipole moments of the ground and excited states is to estimate the Stokes shift itself. The large values of Stokes shifts are predominantly due to the strong intramolecular charge transfer between donating and accepting moieties of molecules.[9] Intramolecular charge transfer states manifest the dipole moments of molecules. In our cases the values ranged from ca. 2 thousand cm^{-1} for C2 up to ca. 5-11 thousand cm^{-1} for C3 totally repeating the order obtained by the theoretical calculations C3>C4>C1>C2.

References

1 L. Onsagbr, *J. Am. Chem. Soc.*, , DOI:10.1021/ja01299a050.
2 N. Mataga, Y. Kaifu and M. Koizumi, *Bull. Chem. Soc. Jpn.*, , DOI:10.1246/bcsj.29.465.
3 S. Sumalekshmy and K. R. Gopidas, *J. Phys. Chem. B*, , DOI:10.1021/jp022549l.
4 E. Lippert, *Zeitschrift fur Naturforsch. - Sect. A J. Phys. Sci.*, , DOI:10.1515/zna-1955-0707.
5 X. Sallenave, A. Bucinskas, S. Salman, D. Volyniuk, O. Bezvikonnyi, V. Mimaite, J. V. Grazulevicius and G. Sini, *J. Phys. Chem. C*, , DOI:10.1021/acs.jpcc.8b02148.
6 N. G. Bakshiev, *Opt Spectosc*, 1964, **16**, 821.
7 G. B. Mathapati, P. K. Ingalagondi, O. Patil, S. B, S. Gounalli and S. M. Hanagodimat, *Int. J. Sci. Res. Phys. Appl. Sci.*, , DOI:10.26438/ijsrpas/v7i2.3843.
8 A. Kawski, P. Bojarski and B. Kukliński, *Chem. Phys. Lett.*, , DOI:10.1016/j.cplett.2008.08.088.
9 K. Shanmugasundaram, M. S. Subeesh, C. D. Sunesh, R. K. Chitumalla, J. Jang and Y. Choe, *J. Phys. Chem. C*, , DOI:10.1021/acs.jpcc.6b04764.

Annex IV.

Charge carrier mobilities are influenced by many factors including molecular packing, disorder, presence of impurities, temperature, electric field, charge-carrier density, size/molecular weight, and pressure. If one focuses on the effect of "disorder" on the charge mobility, the disorder parameter (σ) is a measure of the statistical spread of the electronic interaction of a charged transport molecule with induced dipole moments in the molecular environment, and of the interaction between permanent dipoles of both matrix and transport molecules; the corresponding statistical spread stems from the disordered orientation of dipole moments**.**

These interactions result consequently in a statistical spread of transport-site energies (like in the cartoon shown below), which, in the framework of a gaussian distribution of the site-energy levels, is characterized by the disorder parameter, σ.

As an illustration of this statistical spread of the site energies we provide below a cartoon representation of the impact of the energy disorder on the charge transport: obviously, the obligation for the charge to hop uphill is detrimental for the charge transport as compared to the barrierless hopping in a flat (no disorder) energy landscape.

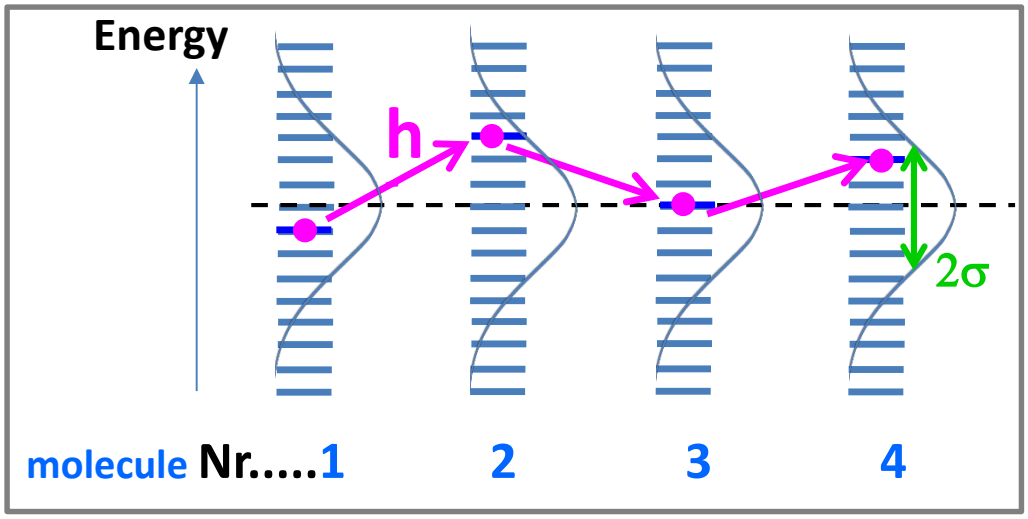

Complete information can be found in: (1) Bässler and Köhler, Top Curr Chem (2012) 312: 1–66 (2) Coropceanu and Bredas, Chem. Rev. 2007, 107, 926-952.

Annex V.

We tried to obtain crystal structures for some of the compounds. We were successful only for one compound, P2, for which a fragment of the crystal structure is shown in Figure S1e. Interestingly, the intermolecular interactions are shown to operate through several hydrogen bonds, which are expected to limit the intermolecular space-overlap to the peripheral fragments. We were able to calculate transfer integrals of the most pertinent pi-pi stacked dimers, and, indeed, the transfer integral values remain very small (Figure S1f). Based on these results, it makes sense to hypothesize that even smaller transfer integrals would be found in the amorphous state of this compound. Again, these results comfort our conclusion that the trends of transfer integrals through the series of compounds C1-C4 and P1-P4 in their amorphous state would not be able to explain the evolution of the corresponding hole mobilities.